https://doi.org/10.5194/egusphere-2023-359
Preprint. Discussion started: 13 June 2023


# Update of the Seismogenic Potential of the Upper Rhine Graben Southern Region

Sylvain Michel[1,2], Clara Duverger[2], Laurent Bollinger[2], Jorge Jara[1], Romain Jolivet[1,3]

[1] Laboratoire de Géologie, Département de Géosciences, Ecole Normale Supérieure, PSL Université, CNRS UMR 8538, 24 Rue Lhomond, 75005, Paris, France.
[2] CEA, DAM, DIF, F-91297 Arpajon, France
[3] Institut Universitaire de France, 1 rue Descartes, 75005, Paris

*Correspondence to*: Sylvain Michel (sylvain_michel@live.fr)

**Abstract.**

The Upper Rhine Graben (URG), located in France and Germany, is bordered by north-south trending faults, some of them considered active, posing a potential threat to dense population and infrastructures from the Alsace plain. The largest historical earthquake in the region is the M6.5+/-0.5 Basel earthquake in 1356. Current seismicity (M>2.5 since 1960) is mostly diffuse and located within the graben. We build upon previous seismic hazard studies of the URG by exploring uncertainties in greater detail, revisiting a number of assumptions. We first take into account the limited evidence of neotectonic activity, then explore tectonic scenarios that have not been taken into account previously, exploring uncertainties on $M_{max}$, its recurrence time, the *b*-value, and the moment released aseismically or through aftershocks. Uncertainties on faults' moment deficit rates, on the observed seismic events' magnitude-frequency distribution, and on the moment-area scaling law of earthquakes are also explored. Assuming a purely dip-slip / normal faulting mechanism associated to a simplified 3 main fault model, $M_{max}$ maximum probability is estimated at $M_w$6.05. Considering this scenario, there would be a 99% probability that $M_{max}$ is below 7.25. In contrast, a strike slip assumption associated to a 4 main fault model, consistent with recent paleoseismological studies and the present day stress field, $M_{max}$ is estimated at $M_w$6.85. Based on this scenario, there would be a 99% probability that $M_{max}$ is less than 7.55.

https://doi.org/10.5194/egusphere-2023-359
Preprint. Discussion started: 13 June 2023


## 1 INTRODUCTION

The Upper Rhine Graben (URG), located in France and Germany, is bounded by north-south trending faults, some of which are considered active, posing a potential threat to the dense population and the industrial and communication infrastructures of the Alsace plain (Figure 1). The largest historical earthquake in the region is the 1356 Basel earthquake with a maximum intensity equal or greater than IX (Mayer-Rosa and Cadiot, 1979; Fäh et al., 2009), an earthquake presently associated to a magnitude between M6.5+/-0.5 (Manchuel et al., 2017) and M6.9+/-0.2 (Fäh et al., 2009). Current seismicity (M>2.5 since 1960) is mostly diffuse and located within the graben (Doubre et al., 2022), hence the difficulty to attribute individual events to a given fault segment. The bordering faults, themselves, are relatively quiet except for the south-eastern section of the graben, near Mulhouse-Basel, where natural seismic sequences (Rouland et al., 1983; Bonjer, 1997) and induced seismicity (Kraft and Deichmann, 2014) has been observed. Seismic activity actually varies along the URG with an increasing rate of events towards the south (Barth et al., 2015). The relative rate between small and large events (b-value from the Gutenberg-Richter law) increases also towards the south indicating a surplus of small earthquakes or a deficit of large events roughly south of Strasbourg (Barth et al., 2015). Focal mechanisms of earthquakes suggest that the region undergoes a strike-slip regime with some normal component (Mazzotti et al., 2021), consistent with the large wavelength strain inferred from geodetic data (Henrion et al., 2020). The characterization of the slip rates of the graben's faults based on geodetic data remains challenging. Indeed regional glacial isostatic adjustments, local subsidence and low tectonic strain rates result in a heterogeneous velocity field with values below 0.2 mm/yr and often within measurement uncertainties (Fuhrmann et al., 2015; Henrion et al., 2020).

The seismic hazard of the URG southern region was recently assessed by Chartier et al. (2017) with a particular focus on the nuclear plant of Fessenheim (Figure 1). This study evaluates the seismic hazard with a fault-based approach, taking into account the network of potentially active fault of Jomard et al. (2017). This fault-based work involves a moment budget approach, which consists in comparing the rate of moment release by seismicity and the rate of moment deficit (MDR) accumulating along locked portions of faults between large earthquakes (i.e. the tectonic loading rate of each fault). Since the period of seismological observation (a few centuries) is too short to be representative of the long-term behavior of seismicity, Chartier et al. (2017) built instead a seismicity model assumed to be representative of the long-term magnitude-frequency distribution (MFD) of earthquakes, a method similarly used in former studies (e.g. Molnar, 1979; Anderson and Luco, 1983; Avouac, 2015). Earthquakes below Mw5 are disregarded (Bommer and Crowley, 2017; Chartier et al., 2017). Earthquakes between Mw5 and 6 are assumed to follow the MFD of the catalog of earthquakes they consider. This catalog integrates several sources of instrumental and historical earthquakes including sources from the *Laboratoire de Détection et de Géophysique* of the *Commissariat à l'Énergie Atomique et aux énergies alternatives* (CEA-LDG; http://www-dase.cea.fr/) and from the FPEC (French Parametric Earthquake Catalogue; Baumont and Scotti, 2011), the IRSN contribution to SHEEC (SHARE European Earthquake Catalogue; Stucchi et al., 2013). The MFDs are estimated within a French seismotectonic zoning scheme defined by Baize et al. (2013). Earthquakes with magnitude above Mw6 are assumed to occur on the fault planes (Jomard et al., 2017). Chartier et al. (2017) consider two types of model: (1) Each fault ruptures only as its maximum magnitude event, which is controlled by the surface area of the seismogenic fault segment (characteristic earthquake model); (2) Events follow the Gutenberg-Richter (GR) law with a b-value equal to 1, and the maximum magnitude, $M_{max}$, is fixed as in the previous model. The recurrence time of the Mw>6 events are then calibrated so that the rate of moment released by the seismicity models matches the MDR estimated from neotectonic data (Chartier et al., 2017; Jomard et al., 2017). The authors explore different fault geometries (e.g. dip and seismogenic depth) using a logic-tree methodology and then proceed to the Probabilistic Seismic Hazard Assessment (PSHA) of the region, providing a map of the probability of exceedance of Peak Ground Acceleration (PGA) within a time period.

Within this framework, a number of strong assumptions are taken. As mentioned previously, a simplified fault network is used (Jomard et al., 2017), which constrains the seismogenic area available for ruptures. Expert choices have also been made to distribute slip rates (i.e. loading rates) originally attributed to faults that have been removed from the initial fault network (Nivière et al., 2008) on other fault segments. On a number of faults, no estimates of neotectonic slip rate are available (e.g. West Rhenish Fault) and the authors have chosen to apply slip rates equivalent to those from other nearby faults (0.01 to 0.05 mm/yr). The neotectonic data are actually only along-dip slip rate estimates. No along-strike slip rates have yet been published due to the lack of markers to quantify horizontal offsets along faults and such component has thus been neglected. In addition, Chartier et al. (2017) do not consider continuous probabilities as they apply a logic-tree method. Chartier et al (2017) fix the b-value to 1, choose the seismogenic depth to be either 15 or 20 km and do not take into account multi-segment ruptures to estimate a $M_{max}$ for each fault segment.

In this study, we build upon Chartier et al. (2017) seismic hazard evaluation of the southern URG by exploring uncertainties in greater detail, revisiting a number of assumptions. We follow the methodology from Rollins and Avouac (2019) and Michel et al. (2021), which allows to evaluate the seismogenic potential of faults in a probabilistic fashion and explore uncertainties on parameters such as the b-value or $M_{max}$. We use the fault

https://doi.org/10.5194/egusphere-2023-359
Preprint. Discussion started: 13 June 2023


network and slip rates taken into account by Nivière et al. (2008), disregarding the Western Rhenish Fault for which slip rate information is unavailable. We assume faults can rupture simultaneously (i.e. multi-segment rupture). In the following sections, we first describe the concepts and methods we use to constrain the seismogenic potential of the URG, then describe the data available before discussing the robustness of our results.

## 2 Method

We follow the methodology from Michel et al. (2021) in order to estimate the seismogenic potential of the upper Rhine Graben, including $M_{max}$ and its recurrence time. As in Chartier et al. (2017), we produce seismicity models representative of the long-term behavior of earthquakes. We assume that background earthquakes have a MFD that follows a Gutenberg-Richter power law up to $M_{max}$. We define background earthquakes as mainshocks, as opposed to their subsequent aftershocks. We assume that their timing of occurrence is random, following a Poisson process. Each model is controlled by three parameters: (1) $M_{max}$, (2) the recurrence time of events of a certain magnitude, $\tau_c$, and (3) the b-value. We use two types of model, namely the tapered and truncated models (Rollins and Avouac, 2019; Michel et al., 2021). The tapered model type assumes a non-cumulative power-law MFD truncated at $M_{max}$, which give rise to a tapered MFD in the cumulative form (i.e. the traditional display when representing the Gutenberg-Richter law). The truncated model type assumes instead a MFD with a distribution truncated at $M_{max}$ in the cumulative form.

The seismicity models are then tested against three constraints: (1) the moment budget, as in Chartier et al. (2017), which implies that moment released by slip on the fault should match the moment deficit accumulating between earthquakes over a long period of time; (2) the moment-area scaling law, an empirical scaling law relating for each earthquake the rupture area to the slip, and (3) the MFD of observed seismicity. In the following sub-sections, we describe in more detail each of those constraints.

### 2.1 Moment budget

A moment budget consists in comparing the rate of moment released from slip events (seismic or aseismic), $\dot{m}_0^{Total}$, with the moment deficit rate, $\dot{m}_0^{def}$, accumulating between slip events. The moment deficit rate is defined by the equation $\dot{m}_0^{def} = \int \mu \ \dot{D}^{def} \ dA$, where $\mu$ is the shear modulus, $A$ is the area that remains locked during the interseismic period (i.e. the potential seismogenic zone), and $\dot{D}^{def}$ is the rate at which slip deficit builds up. Since it is not yet possible in the URG to determine the distribution of locked segments of faults and their associated loading rates from geodetic measurements, $A$ is assumed homogeneous along-strike for each fault, while we

https://doi.org/10.5194/egusphere-2023-359
Preprint. Discussion started: 13 June 2023


consider possible the seismogenic width to change from one fault to another. The rate at which slip deficit builds up, $\dot{D}^{def}$, is evaluated based on neotectonic information (see Section 3.1). The total moment released, $\dot{m}_0^{Total}$ is calculated based on the rate of moment release of the long-term seismicity model. Since, the long-term seismicity model considers only mainshocks, we include a fourth parameter, $\alpha_s$, that represents the proportion of moment released by background seismicity, $m_0^{Bckgrd}$, relative to the total moment released (including aftershocks and aseismic afterslip). If $\dot{m}_0^{def} = \dot{m}_0^{Total} = \dot{m}_0^{Bckgrd} / \alpha_s$, then the moment budget is said to be balanced.

The cumulative MFD of tapered and truncated seismicity models that balances the moment budget have an analytical form and are a function of $M_{max}, b, \dot{m}_0^{def}$ and $\alpha_s$ (see Rollins and Avouac, 2019, and references therein). We can therefore estimate the probability of a seismicity model balancing the moment budget, $P_{Budget}$, by sampling the *a priori* distributions of those parameters.

### 2.2 Moment-area scaling law

According to global earthquake statistics, the moment released by an earthquake, $\mathrm{m}_0^{Seis}$, is proportional to the area of its rupture, $A_{eq}$, such as $m_0^{seis} \propto A_{eq}^{3/2}$ (Wells and Coppersmith, 1994; Leonard, 2010; Stirling et al., 2013). We use this scaling to evaluate whether a seismic event of a given magnitude has a rupture area that fits within the seismogenic zone. By considering the spread on the empirical distribution of magnitude vs. area, we assume the probability distribution function of an event of magnitude $M_w$ to be probable considering this scaling, $P_{scaling}$. We use here the self-consistent scaling law, and related uncertainties, as defined by Leonard (2010) in its dip-slip equation (the strike-slip equation is in any case almost the same).

### 2.3 Earthquake catalog

We finally test whether the observed MFD from earthquake catalogs may be a sample of the distribution of the long-term seismicity models we are building. Effectively, we evaluate the likelihood of our observed MFD given the distribution of the models. Since we consider here only mainshocks. We define the likelihood of the observed seismicity catalog, $P_{Cat}$, as $P_{Cat} = \prod_i P_{poisson}^{M_i}$, where $P_{poisson}^{M_i}$ is the probability to observe $n_{obs}^{M_i}$ events, within the magnitude bin $M_i$, occurring during the time period $t_{obs}^{M_i}$, assuming the long-term mean recurrence of events is $\tau_{model}^{M_i}$:

$$P_{poisson}^{M_i}\left(n_{obs}^{M_i}, t_{obs}^{M_i}, \tau_{model}^{M_i}\right) = \frac{\left(t_{obs}^{M_i}/\tau_{model}^{M_i}\right)^{n_{obs}^{M_i}}}{\left(n_{obs}^{M_i}\right)!} e^{-t_{obs}^{M_i}/\tau_{model}^{M_i}}.$$

https://doi.org/10.5194/egusphere-2023-359
Preprint. Discussion started: 13 June 2023


Effectively, for a given seismicity model, we generate randomly 2500 declustered catalogs of earthquakes. We evaluate the likelihood of each catalog and define $P_{Cat}$ as the average of these likelihood values.

Note that we follow the recommendation from Felzer (2008) while exploring magnitude uncertainties and correct for each event their magnitude by $\Delta M = (b^2\sigma^2)/(2\ log_{10}(e))$, where $b$ is the declustered catalog $b$-value, $\sigma$ is the standard deviation of the event's magnitude, and $e$ is the exponential constant.

### 2.4 Seismicity model probability and marginal probabilities

Finally, the probability of a seismicity model is defined as $P_{SM} = P_{Budget}\ P_{Cat}\ P_{scaling}\ P_{Barriers}$ which depends, among others, on $M_{max}$ and $b$ (Michel et al., 2021). Marginal probabilities such as $P_{M_{max}}$, the probability of $M_{max}$, and $P_b$, the $b$-value probability, can be estimated based on $P_{SM}$. We also define $P(\tau_{max} \mid M_{max})$ as the probability of the rate of $M_{max}$, and $P(\tau \mid M_w)$ as the probability of the rate of events with magnitude $M_w$, which accounts for all earthquakes from all of the models (i.e. not only $M_{max}$). Probabilities needed for estimating seismic hazard (e.g. PSHA) such as the probability to have an event above magnitude $M_w$ for a time period $T$, $P(M > M_w \mid T)$, can likewise be evaluated.

## 3 Data and associated uncertainties

We present in this section the data and their associated uncertainties used to evaluate each constraint.

### 3.1 Neotectonic data, seismogenic along-dip width and moment deficit rate

To evaluate the MDR for the moment budget constraint (Section 2.1), we must infer estimates of loading rate (i.e. $\dot{D}^{def}$) for each fault taken into account. The slip rate on each fault is taken from Nivière et al. (2008) for the Rhine River, Black Forest, Weinstetten and Lehen-Schonberg faults (the Landeck or West Renish faults are not considered). Their slip rates rely on estimates of the cumulative vertical displacement of the faults based on Pliocene-Quaternary sediments thickness variations measured from 451 boreholes, assuming that the accommodation space opened by tectonic motion is completely balanced (or over-balanced) by sedimentation. However, potential erosional periods due to the piracy of the Rhine River might bias the measurements, thus the values are to be interpreted as maximum displacement estimates. From the age of the sediments, Nivière et al. (2008) infer vertical slip rates of 0.07 and 0.17 mm/yr for the Rhine River and Weinstetten faults, respectively. The Lehen-Schonberg fault slip is given between 0.04 and 0.1 mm/yr. While borehole observations do not allow to conclude on the Pliocene-Quaternary slip rate of the Black Forest fault, this structure is suggested to be inactive

https://doi.org/10.5194/egusphere-2023-359
Preprint. Discussion started: 13 June 2023


during this time period, and that the deformation is now accommodated by the other faults aforementioned (Nivière et al., 2008). Note that those are vertical slip rate estimates and that the along-strike component is for the moment neglected. For the moment rate calculation, we project vertical slip rates on the along-dip direction considering the dip angles of each fault.

The seismogenic down-dip extent of a fault depends on the temperature gradient (e.g. Oleskevich et al., 1999), among other parameters. Indeed, between the isotherms 350°C and 450°C, quartzo-feldspathic rocks undergo a transition in frictional properties (Blanpied et al., 1995) from a rate-weakening (<350°C), potentially seismogenic behavior to a rate-strengthening (>450°C), stable sliding behavior (Dieterich, 1979; Ruina, 1983). The geothermal gradient below the URG is higher than the surrounding regions due to its tectonic history (Freymark et al., 2017). Based on borehole temperature measurements from Guillou-Frottier et al. (2013), we estimate the envelopes of the geothermal gradient in the southern URG (Figure S1) and show that the frictional property transition would occur between 6 and 18 km depth. In this study, we define the PDF of the seismogenic down-dip extent as a uniform distribution between 0 and 6 km depth associated to a linear taper down to 18 km. The linearity of the taper within the transition zone is not physic-driven and has been chosen arbitrarily.

Additionally, the southern part of the URG is the location of a potash-salt evaporitic basin (Lutz and Cleintuar, 1999; Hinsken et al., 2007; Freymark et al., 2017), which reaches a maximum depth of ~2 km. Such formation may not accumulate any moment deficit as the yield stress of evaporites is very low (Carter and Hansen, 1983). We assume each fault is potentially impacted by this formation, hence modulating the seismogenic thickness and in turn the seismogenic area available for a rupture. The resulting PDF of the seismogenic thickness is the convolution of the PDF of the down-dip extent of the seismogenic zone with the PDF of the evaporitic basin thickness, a uniform distribution between 0 and 2 km. The combination of both temperature and salt basin assumptions leads to a PDF of the along-dip seismogenic width, which is uniform down to ~5 km and decreases linearly until ~17 km (Figures S2 to S5).

The moment deficit is then the product between the length of each fault, their seismogenic width, the neo-tectonic long-term slip rate, and the shear modulus that we fix to 30 GPa (same as in Chartier et al., 2017). Each fault is assumed to have its own seismogenic width. The moment deficit rate of each fault is shown in Figure 1. The PDFs of each of the fault's constitutive parameters are shown in Figure S2 to S5. Considering the range of the fault's geometrical parameters, which considers also the Black Forest Fault even though it is assumed to be non-active,

https://doi.org/10.5194/egusphere-2023-359
Preprint. Discussion started: 13 June 2023


we obtain the moment-area constraint shown in Figure 2. Until $M_w$6.5, events are equiprobable while those above $M_w$7.7 are extremely improbable.

### 3.2 Instrumental and historical seismicity catalogs

We use the earthquake catalog from Drouet et al. (2020) to constrain the MFD of the long-term seismicity models (Section 2.3). This catalog was built from multiple former catalogs. It relies mostly on the FCAT-17 catalog (Manchuel et al., 2018), which is itself a combination of the instrumental catalog SiHex (SIsmicité de l'HEXagone; Cara et al., 2015) for the 1965-2009 period, and an historical catalog based on the macroseismic database of SISFRANCE (BRGM, IRSN, EDF), intensity prediction equations from Baumont et al. (2018) and the macroseismic moment magnitude determination from Traversa et al. (2018) for the 463-1965 period. Events beyond 20 km of the French border, not provided by the FCAT-17, are based on the SHEEC catalog (Stucchi et al., 2013; Woessner et al., 2015). Finally, events from 2010 to 2016 come from the CEA-LDG bulletins (https://www-dase.cea.fr). All events magnitude are given in $M_w$ and uncertainties are provided. Anthropic events are expected to be already removed from the catalog (Cara et al., 2015; Manchuel et al., 2018).

We select events within the coordinates [6°,8.5°] in longitude and [47°,49.5°] latitude, a broad region covering the whole URG, and divide the catalog in two time periods, an instrumental and an historical one taking events from 1980 onwards and 1850 onwards, respectively. We decluster both catalogs to compare them to the long-term seismicity models (Section 2.3). Declustering is based on the methodology of Marsan et al. (2017), which evaluates the probability that an earthquake is a mainshock. Declustering is applied based on a completeness magnitude, $M_c$, of 2.2 and 3.2 for the instrumental and historical catalogs, respectively (Text S1; Figures S6 and S7). From the resulting catalogs, we keep events from 1994 onwards and 1860 onwards for the instrumental and historical catalog, respectively (Figures S6 and S7), in order to avoid border effects from declustering. For the instrumental catalog, 1994 is also the date from which seismicity rate appears relatively constant (Figure S6). We then select events in the region of interest (i.e. the southern part of the URG), taking into account only earthquakes located within a 10 km buffer around the faults considered, including the Black Forest fault (Figure 3). Note that since no events are considered below $M_c$, there is a lack of events which falls in the magnitude bins directly above $M_c$ while exploring magnitude uncertainties. Thus, when applying the earthquake catalog constraint (Section 2.3), we take events with $M_w > 2.75$ and $M_w > 4.25$ for the instrumental and historical catalogs, respectively (Felzer, 2008) (Figure 3).

### 3.3 Seismicity model constitutive parameters

https://doi.org/10.5194/egusphere-2023-359
Preprint. Discussion started: 13 June 2023


As mentioned in Section 2.1, the cumulative MFD of tapered and truncated seismicity models balancing the moment budget can be defined as a function of $M_{max}$, $b$, $\dot{m}_0^{def}$ and $\alpha_s$. We explore those parameters through a grid search with $M_{max}$ and $b$ sampled uniformly over $M_{max} \in \mathcal{U}(4.5{,}9.9)$ and $b \in \mathcal{U}(0.1{,}1.45)$, respectively. Based on global statistics of the post-seismic response following earthquakes (Alwahedi and Hawthorne, 2019; Churchill et al., 2022), we assume the PDF of $\alpha_s$ is a Gaussian distribution with $\mathcal{N}(90\%, 25\%)$ (Figure S8). Finally, the PDF of the MDR of each fault is assumed uniform between 0 and the estimate based on the maximum slip rate from Nivière et al. (2008) (Section 3.1). We thus include scenarios for which almost no moment deficit accumulates on the fault (i.e. the fault slips aseismically or accommodates no strain over long periods of time). This hypothesis contrasts with the choice from Chartier et al. (2017) who assume each fault is fully locked over a seismogenic width terminating at either 15 or 20 km. Doing so, we explore a broad range of possible models.

## 4 Results

The combination of constraints (Section 2) leads to the results shown in Figure 4. For the truncated model, the marginal probability of $P_{SM}$ in the $M_{max}$ and $\tau_{max}$ is represented by the gray shaded distribution in Figure 4 (not shown for the tapered model since the models taper at $M_{max}$). The marginal probability of $M_{max}$ for the tapered model (in green) peaks at 6.05, while the one for the truncated model (in blue) is bi-modal with peaks at 5.15 and 5.75. For the truncated model (not the tapered model for the same reason as previously indicated), the marginal probability $P(\tau_{max} \mid M_{max} = 5.75)$ (solid blue line in the y-axis) peaks at ~1000 yrs. Taking $M_{max}$ =6.55 or 6.95, a number close to the estimated magnitude of the 1356 Basel earthquake, the marginal probability would instead peak at ~16,000 and ~80,000 yrs, respectively.

The marginal probabilities $P(\tau \mid M_w = 6.05)$ and $P(\tau \mid M_w = 5.75)$ for the tapered and truncated models (green and blue dotted lines on the y-axis, respectively), which take all events of the seismicity models into account (not only $M_{max}$), have instead peaks at ~16,000 yrs and ~10,000 yrs, respectively. The marginal probability $P_b$ peaks at ~0.85 and 0.9 for the tapered and truncated models, respectively.

The effect with and without the moment-area scaling law is shown in Figure 5. Adding the scaling law constraint does not change the mode of $P_{M_{max}}$ but completely rejects scenarios with $M_{max}$>7.8.

Finally, the probabilities $P(M > M_w \mid T)$ for $T = 100$ and 10,000 yrs are also shown in Figure 5. As an example, the probability of occurrence for an event above $M_w$6.5 (similar to the 1356 Basel earthquake) for an observational

https://doi.org/10.5194/egusphere-2023-359
Preprint. Discussion started: 13 June 2023


period of 100 yrs is ~0.1% for both the tapered and truncated models. For an event above $M_w$6.0 and for the same period, it is instead ~1% for both models (see zoom in Figure 5.c).

# 5 Discussion

## 5.1 Sensibility to earthquake catalog declustering

The catalog declustering (i.e. removal of aftershocks) may have a significant impact on the results (Section 2.3), influencing the shape of the observed MFD of earthquakes. We use in this study the methodology from Marsan et al. (2017), which is based on ETAS framework and intrinsically assumes that background events have a Poisson behavior. Other declustering methodologies are available and we test here the one from Zaliapin and Ben-Zion (2013) based on nearest-neighbor distances of events in space-time-energy domain. The results from this methodology produce background seismicity catalogs with more events than the one from Marsan et al. (2017) (Text S2 and Figures S9 to S11), but infers larger b-values when combining the instrumental catalog with the historical one (as inferred by Figure 6.b). The analysis on the seismogenic potential of the URG using Zaliapin and Ben-Zion (2013) methodology results with $P_{M_{max}}$ peaking at M6.25 for the tapered model, and still being bi-modal for the truncated model, with peaks at M5.15 and M5.85 (Figure 6). Unlike with Marsan et al. (2017), the second peak for the truncated model is more probable than the first one. The most probable $M_{max}$ for both models are thus slightly higher than the ones estimated using Marsan et al. (2017) methodology. The resulting marginal probabilities $P(\tau \mid M_w = 6.15)$ and $P(\tau \mid M_w = 5.85)$ for the tapered and truncated models have peaks at ~25,000 yrs and ~12,500 yrs, respectively.

## 5.2 Source of seismicity

We initially selected earthquakes within a 10 km buffer around the faults as it reflects the strain spatial pattern of a vertical fault blocked down to 10 km depth. Nevertheless, the locking depth could potentially be deeper, down to ~18 km as suggested in Section 3.1. We thus also provide the results selecting events within 20 km from the faults (Figures S12 and S13). Under these conditions, seismicity rates of the observational earthquake catalogs are higher and thus constrain the long-term seismicity models to cases that produce higher moment release rate. $P_{M_{max}}$ favours thus events of lower magnitude than the one using events within 10 km (Figure 5; Section 4). The tapered model peaks at $M_w$5.85, instead of 6.05, while the truncated model has two peaks at $M_w$5.15 and 5.75, very similar to the reference scenario in Section 4, except that the peak at $M_w$5.15 is now the most probable.

https://doi.org/10.5194/egusphere-2023-359
Preprint. Discussion started: 13 June 2023


However, current seismicity in the URG is seemingly diffuse and it is difficult to associate it with a fault in particular (Doubre et al., 2022). On the other hand geodetic data are not yet able to resolve any tectonic deformation and thus to evaluate the loading rate of faults (Henrion et al., 2020). Even though the Drouet et al. (2020) catalog, based on FCAT-17 catalog, is supposedly devoid of anthropic seismicity (Cara et al., 2015; Manchuel et al., 2018), one can then ask whether the current seismicity is totally representative of the undergoing long-term tectonic processes or presently modulated by surface loads such as the post-glacial rebound (e.g. Craig et al., 2016), aquifer loads, erosion or incision (e.g. Bettinelli et al., 2008; Steer et al., 2014; Craig et al., 2017). If so, the hypothesis stating that the main driver of seismicity is tectonic loading breaks down and our method for assessing seismic hazard must be completed by physics-based constraints of such transient stress release (Calais et al., 2016). Distinguishing seismic sources triggered by tectonic loading from other driven forces is an extremely difficult task. The earthquake catalog contribution (Section 2.3) might then not be appropriate.

Additionally, the magnitude of historical events from the FCAT-17 catalog (before the 1960s), and thus the one from Drouet et al. (2020), seem to be overestimated (or instead the instrumental events have underestimated magnitudes even though it seems less probable) and a bias of the MFD is thus expected (Beauval and Bard, 2022; Doubre et al., 2022). For the URG case, 3 bins out of 7 of the observed MFD are estimated from the instrumental period. The ones estimated from the historical period have thus slightly more weight in the catalog constraint (Section 2.3).

We test an alternative constraint inferring that the possible magnitude and frequency of $M_{max}$ must be consistent with the observed largest event over the observation period (~146 yrs), meaning that it has to be larger than or equal to the known largest event while the return period of the largest event cannot be significantly smaller than the observation period (Approach 2 from Michel et al., 2018). This constraint is equivalent to consider that there is no earthquakes of magnitude over the largest event seen in the observation period occurring during the time period of the observed catalog. Theoretically, this constraint imposes a lower bound on $M_{max}$ and its recurrence time. The results using this constraint together with the moment budget and scaling law ones are shown in Figure 7. Since $M_{max}$ frequency is different between the tapered and truncated models, the new constraint imposes different lower bounds on the two models, the truncated model rejecting more strongly scenarios with $M_{max}$ below M5.5. $P_b$ is not constrained by the observed seismicity catalog but higher values of the b-value seem slightly more probable (inset of Figure 7). The marginal probabilities $P(\tau \mid M_w = 5.85)$ and $P(\tau \mid M_w = 6.25)$ for the tapered and truncated models have peaks at ~12,500 yrs and ~63,000 yrs, respectively.

https://doi.org/10.5194/egusphere-2023-359
Preprint. Discussion started: 13 June 2023


### 5.3 Strike slip component

In this study, as well as in Chartier et al. (2017), we assume solely along-dip displacement since it is the only published neo-tectonic information available. Nevertheless, recent paleo-seismological data on the Black Forest fault suggest 2 m of strike-slip, in contrast to 0.3-0.6 m of vertical slip, for an event that occurred after the last glacial maximum (~15,000 yrs) (Abstract Castellnou et al., 2022, from PATA days and personal communication from Castellnou). There are also evidence of other events with left-lateral slip, associated with vertical 0.5 m displacement. It suggest (1) that the Black Forest fault has been active during the Quaternary period and that (2) strike-slip might be predominant. The ratio between strike- and dip-slip from the Black Forest event would be then between 3.3 and 6.6. We thus test a scenario where the Black Forest fault is associated with a maximum vertical slip deficit rate of 0.18 mm/yr, as proposed by Jomard et al. (2017), and where we multiply the maximum slip deficit rate of all considered faults by 6.6 (the largest strike- over dip-slip ratio suggested). The results and the revised MDR of each fault are shown in Figures 8 and S14. $P_{M_{max}}$ peaks at M6.85 and M6.65 for the tapered and truncated models, respectively. They are associated with the marginal probabilities $P(\tau \mid M_w = 6.85)$ and $P(\tau \mid M_w = 6.65)$ that both peak at ~16,000 yrs for the tapered and truncated models, respectively. Note that using Wells and Coppersmith (1994) equation between moment magnitude and average slip/maximum slip, the 2 m amount of strike-slip estimated by Castellnou et al. (2022) would suggest a $\sim M_w 7.3/7.0$. $P_b$ peaks at 0.65 and 0.7 for the tapered and truncated models, respectively, thus at lower values than taking into account the vertical-slip component alone.

The previous scenario tested (Figure 8) takes two more faults (i.e. Weinstetten and Lehen-Schonberg faults) into account than in Chartier et al. (2017), as those two faults are not present within the BDFA (the French database of potentially active faults; Jomard et al., 2017). The results following Chartier et al. (2017) fault selection and applying the strike slip assumption are provided in Figure S15. $P_{M_{max}}$ peaks at M6.75 and M6.55 for the tapered and truncated models, respectively, very similar to the scenario taking all four faults, as the moment deficit rate is dominated by the Rhine River and Black Forest faults. Note that the marginal probabilities $P(\tau \mid M_w)$ and $P(\tau_{max} \mid M_{max})$ seem to get more noisy, likely due to the shape of the MDR PDF which skews heavily towards zero (black line in Figure S14.e).

### 5.4 Multi-segment rupture

https://doi.org/10.5194/egusphere-2023-359
Preprint. Discussion started: 13 June 2023


In this study we assume that all faults can rupture simultaneously. Nevertheless, the Black Forest Fault is initially taken as none active, and the traces of the Weinstetten and Lehen-Schonberg faults are separated by a minimum of 7.9 km. According to Wesnousky (2006), multi-segment ruptures are associated to low probability when the inter segment distance exceeds 5 km. Consequently, the seismogenic potential scenario from Section 4 would then be an overestimation. On the other hand, according to Castellnou et al., 2022, the Black Forest Fault is in fact active and seismogenic, and could be assumed to rupture with other faults. Additional structures might actually link all the faults together (e.g. Lutz and Cleintuar, 1999; Bertrand et al., 2006; Rotstein and Schaming, 2011). In this case, the seismogenic potential scenario from Section 4 would be interpreted as an underestimation.

Finally, we only consider the faults within a finite zone, which controls the total seismogenic area of the faults (i.e. the moment-area scaling law effect), whereas the faults continue northwards and southwards to a lesser extent. According to Weng and Yang (2017), the aspect ratio (rupture's width over length) of dip-slip events almost doesn't reach beyond 8. Taking a seismogenic width of 18 km (our maximum estimate), the maximum length of earthquakes would then be 144 km, while the full length of the URG considered faults, Black Forest fault included, is ~250 km (~160 km if the Black Forest fault is not included). The rupture of all the faults would then be unlikely. On the other hand, strike-slip events do not seem to be capped by any aspect ratio (Weng and Yang, 2017), so $M_w$>7.5 events cannot then be excluded in this context.

## 6 Conclusion

In this study, we investigate the seismogenic potential of the south-eastern URG, building upon the work from Chartier et al. (2017). Based on a complex fault network (Nivière et al., 2008), we evaluate scenarios that have not been accounted for previously, exploring uncertainties on $M_{max}$, its recurrence time, the *b*-value, and the moment released aseismically or through aftershocks. Uncertainties on the MDR, the observed MFD, and on the moment-area scaling law are also explored. Given the four faults considered, and the scenario in which the Black Forest fault is no longer active but where the other faults can still rupture simultaneously, the $M_{max}$ maximum probability is estimated at $M_w$6.05 and $M_w$5.75 using the tapered or the truncated seismicity models, respectively. Nevertheless, $P_{M_{max}}$ for the truncated model has a second peak at $M_w$5.15 and the recurrence time of events of such magnitude (not only $M_{max}$), $P(\tau \mid M_w = 5.15) \sim 2{,}000$ yrs, is much lower than the one estimated using the main peak, $P(\tau \mid M_w = 5.75) \sim 10{,}000$ yrs. Still considering the scenario ignoring the Black Forest fault, there would be a 99% probability that $M_{max}$ is below 7.25 using either the tapered or truncated model. In contrast,

https://doi.org/10.5194/egusphere-2023-359
Preprint. Discussion started: 13 June 2023


considering strike-slip as described in Section 5.3 and taking the Black Forest Fault into account, there would be a 99% probability that $M_{max}$ is below 7.55 for both models.

In any case, within this study, strong assumptions still had to be made that certainly affect the results. It includes the methodology used to decluster the earthquake catalogs, on whether a comparison between the loading rate of each fault and seismicity is wise, on considering only the dip-slip component while strike-slip is highly probable, on the possibility of multi-segment ruptures and even the choice of the faults to consider. Further work, from paleo-seismology, seismic reflection, geodesy, or earthquake relocation is needed to extract more information on the structures tectonically involved and their associated loading rate, and to better constrain the URG seismic hazard. Longer time series on all the fields mentioned above might also help in this matter.

## 7 Code Availability

## 8 Data Availability

## 9 Author Contrubution

## 10 Competing Statement

The authors acknowledge there are no conflicts of interest recorded.

## 11 Acknowledgement

This work received funding from the European Research Council (ERC) under the European Union's Horizon 2020 research and innovation program (Geo-4D project, grant agreement 758210). RJ acknowledges funding from the Institut Universitaire de France.

https://doi.org/10.5194/egusphere-2023-359
Preprint. Discussion started: 13 June 2023


## 12 References


Alwahedi, M. A., and J. C. Hawthorne, 2019, Intermediate-Magnitude Postseismic Slip Follows Intermediate-Magnitude ( M 4 to 5) Earthquakes in California, Geophys. Res. Lett., 46, no. 7, 3676–3687, doi: 10.1029/2018GL081001.

Anderson, J. G., and J. E. Luco, 1983, Consequences of slip rate constraints on earthquake occurrence relations, Bull. - Seismol. Soc. Am., 73, no. 2, 471–496, doi: https://doi.org/10.1785/BSSA0730020471.

Avouac, J.-P., 2015, From Geodetic Imaging of Seismic and Aseismic Fault Slip to Dynamic Modeling of the Seismic Cycle, Annu. Rev. Earth Planet. Sci., 43, doi: 10.1146/annurev-earth-060614-105302.

Baize, S., E. M. Cushing, F. Lemeille, and H. Jomard, 2013, Updated seismotectonic zoning scheme of Metropolitan France, with reference to geologic and seismotectonic data, Bull. la Société Géologique Fr., 184, no. 3, 225–259, doi: 10.2113/gssgfbull.184.3.225.

Barth, A., J. R. R. Ritter, and F. Wenzel, 2015, Spatial variations of earthquake occurrence and coseismic deformation in the Upper Rhine Graben, Central Europe, Tectonophysics, 651–652, 172–185, doi: 10.1016/j.tecto.2015.04.004.

Baumont, D., K. Manchuel, P. Traversa, C. Durouchoux, E. Nayman, and G. Ameri, 2018, Intensity predictive attenuation models calibrated in Mw for metropolitan France, Bull. Earthq. Eng., 16, no. 6, 2285–2310, doi: 10.1007/s10518-018-0344-6.

Beauval, C., and P. Bard, 2022, History of probabilistic seismic hazard assessment studies and seismic zonations in mainland France, Comptes Rendus. Géoscience, 353, no. S1, 413–440, doi: 10.5802/crgeos.95.

Bertrand, G., P. Elsass, G. Wirsing, and A. Luz, 2006, Quaternary faulting in the Upper Rhine Graben revealed by high-resolution multi-channel reflection seismic, Comptes Rendus Geosci., 338, no. 8, 574–580, doi: 10.1016/j.crte.2006.03.012.

Bettinelli, P., J. P. Avouac, M. Flouzat, L. Bollinger, G. Ramillien, S. Rajaure, and S. Sapkota, 2008, Seasonal variations of seismicity and geodetic strain in the Himalaya induced by surface hydrology, Earth Planet. Sci. Lett., 266, nos. 3–4, 332–344, doi: 10.1016/j.epsl.2007.11.021.

Blanpied, M. L., D. A. Lockner, and D. Byedee, 1995, Frictional slip of granite at hydrothermal conditions, J. Geophys. Res., 100, no. B7, 13,045-13,064.

Bommer, J. J., and H. Crowley, 2017, The Purpose and Definition of the Minimum Magnitude Limit in PSHA Calculations, Seismol. Res. Lett., 88, no. 4, 1097–1106, doi: 10.1785/0220170015.

Bonjer, K.-P., 1997, Seismicity pattern and style of seismic faulting at the eastern borderfault of the southern Rhine Graben, Tectonophysics, 275, nos. 1–3, 41–69, doi: 10.1016/S0040-1951(97)00015-2.

Calais, E., T. Camelbeeck, S. Stein, M. Liu, and T. J. Craig, 2016, A new paradigm for large earthquakes in stable continental plate interiors, Geophys. Res. Lett., 43, no. 20, 10,621-10,637, doi: 10.1002/2016GL070815.

Cara, M. et al., 2015, SI-Hex: a new catalogue of instrumental seismicity for metropolitan France, Bull. la Société Géologique Fr., 186, no. 1, 3–19, doi: 10.2113/gssgfbull.186.1.3.

Carter, N. L., and F. D. Hansen, 1983, Creep of rocksalt, Tectonophysics, 92, no. 4, 275–333, doi: 10.1016/0040-1951(83)90200-7.

Castellnou, S. P., J. Hürtgen, S. Baize, and K. Reicherter, 2022, Paleoseismic characterization of the eastern Rhine Graben Boundary Fault (RGFB), Southern Germany, in *International workshop on Paleoseismology, Active Tectonics, and Archaeoseismology*.

Chartier, T., O. Scotti, C. Clément, H. Jomard, and S. Baize, 2017, Transposing an active fault database into a fault-based seismic hazard assessment for nuclear facilities – Part 2: Impact of fault parameter uncertainties on a site-specific PSHA exercise in the Upper Rhine Graben, eastern France, Nat. Hazards Earth Syst. Sci., 17, no. 9, 1585–1593, doi: 10.5194/nhess-17-1585-2017.

https://doi.org/10.5194/egusphere-2023-359
Preprint. Discussion started: 13 June 2023


Churchill, R. M., M. J. Werner, J. Biggs, and Å. Fagereng, 2022, Afterslip Moment Scaling and Variability From a Global Compilation of Estimates, J. Geophys. Res. Solid Earth, 127, no. 4, doi: 10.1029/2021JB023897.

Craig, T. J., E. Calais, L. Fleitout, L. Bollinger, and O. Scotti, 2016, Evidence for the release of long-term tectonic strain stored in continental interiors through intraplate earthquakes, Geophys. Res. Lett., 43, no. 13, 6826–6836, doi: 10.1002/2016GL069359.

Craig, T. J., K. Chanard, and E. Calais, 2017, Hydrologically-driven crustal stresses and seismicity in the New Madrid Seismic Zone, Nat. Commun., 8, no. 1, 2143, doi: 10.1038/s41467-017-01696-w.

Dieterich, J. H., 1979, Modeling of Rock Friction Experimental Results and Constitutive Equations, J. Geophys. Res., 84, no. B5, 2161–2168.

Doubre, C., M. Meghraoui, F. Masson, S. Lambotte, H. Jund, M. Bès de Berc, and M. Grunberg, 2022, Seismotectonics in Northeastern France and neighboring regions, Comptes Rendus. Géoscience, 353, no. S1, 153–185, doi: 10.5802/crgeos.80.

Drouet, S., G. Ameri, K. Le Dortz, R. Secanell, and G. Senfaute, 2020, A probabilistic seismic hazard map for the metropolitan France, Bull. Earthq. Eng., 18, no. 5, 1865–1898, doi: 10.1007/s10518-020-00790-7.

Fäh, D. et al., 2009, The 1356 Basel earthquake: an interdisciplinary revision, Geophys. J. Int., 178, no. 1, 351–374, doi: 10.1111/j.1365-246X.2009.04130.x.

Felzer, K. R., 2008, Calculating California seismicity rates.

Freymark, J., J. Sippel, M. Scheck-Wenderoth, K. Bär, M. Stiller, J.-G. Fritsche, and M. Kracht, 2017, The deep thermal field of the Upper Rhine Graben, Tectonophysics, 694, 114–129, doi: 10.1016/j.tecto.2016.11.013.

Fuhrmann, T., M. Caro Cuenca, A. Knöpfler, F. J. van Leijen, M. Mayer, M. Westerhaus, R. F. Hanssen, and B. Heck, 2015, Estimation of small surface displacements in the Upper Rhine Graben area from a combined analysis of PS-InSAR, levelling and GNSS data, Geophys. J. Int., 203, no. 1, 614–631, doi: 10.1093/gji/ggv328.

Guillou-Frottier, L., C. Carrė, B. Bourgine, V. Bouchot, and A. Genter, 2013, Structure of hydrothermal convection in the Upper Rhine Graben as inferred from corrected temperature data and basin-scale numerical models, J. Volcanol. Geotherm. Res., 256, 29–49, doi: 10.1016/j.jvolgeores.2013.02.008.

Heidbach, O. et al., 2018, The World Stress Map database release 2016: Crustal stress pattern across scales, Tectonophysics, 744, 484–498, doi: 10.1016/j.tecto.2018.07.007.

Heidbach, O., M. Rajabi, K. Reiter, M. O. Ziegler, and WSM Team, 2016, World Stress Map Database Release 2016, V. 1.1. GFZ Data Services.

Henrion, E., F. Masson, C. Doubre, P. Ulrich, and M. Meghraoui, 2020, Present-day deformation in the Upper Rhine Graben from GNSS data, Geophys. J. Int., 223, no. 1, 599–611, doi: 10.1093/gji/ggaa320.

Hinsken, S., K. Ustaszewski, and A. Wetzel, 2007, Graben width controlling syn-rift sedimentation: the Palaeogene southern Upper Rhine Graben as an example, Int. J. Earth Sci., 96, no. 6, 979–1002, doi: 10.1007/s00531-006-0162-y.

Jomard, H., E. M. Cushing, L. Palumbo, S. Baize, C. David, and T. Chartier, 2017, Transposing an active fault database into a seismic hazard fault model for nuclear facilities – Part 1: Building a database of potentially active faults (BDFA) for metropolitan France, Nat. Hazards Earth Syst. Sci., 17, no. 9, 1573–1584, doi: 10.5194/nhess-17-1573-2017.

Kraft, T., and N. Deichmann, 2014, High-precision relocation and focal mechanism of the injection-induced seismicity at the Basel EGS, Geothermics, 52, 59–73, doi: 10.1016/j.geothermics.2014.05.014.

Leonard, M., 2010, Earthquake Fault Scaling: Self-Consistent Relating of Rupture Length, Width, Average Displacement, and Moment Release, Bull. Seismol. Soc. Am., 100, no. 5A, 1971–1988, doi: 10.1785/0120090189.

https://doi.org/10.5194/egusphere-2023-359
Preprint. Discussion started: 13 June 2023


Lutz, M., and M. Cleintuar, 1999, Geological results of a hydrocarbon exploration campaign in the southern Upper Rhine Graben (Alsace Centrale, France), Bull. für Angew. Geol., 4, 3–80, doi: http://doi.org/10.5169/seals-221515.

Manchuel, K., P. Traversa, D. Baumont, M. Cara, E. Nayman, and C. Durouchoux, 2018, The French seismic CATalogue (FCAT-17), Bull. Earthq. Eng., 16, no. 6, 2227–2251, doi: 10.1007/s10518-017-0236-1.

Marsan, D., M. Bouchon, B. Gardonio, H. Perfettini, A. Socquet, and B. Enescu, 2017, Change in seismicity along the Japan trench, 1990-2011, and its relationship with seismic coupling, J. Geophys. Res. Solid Earth, 122, no. 6, 4645–4659, doi: 10.1002/2016JB013715.

Mayer-Rosa, D., and B. Cadiot, 1979, A review of the 1356 Basel earthquake: Basic data, Tectonophysics, 53, nos. 3–4, 325–333, doi: 10.1016/0040-1951(79)90077-5.

Mazzotti, S. et al., 2021, FMHex20: An earthquake focal mechanism database for seismotectonic analyses in metropolitan France and bordering regions, BSGF - Earth Sci. Bull., 192, 10, doi: 10.1051/bsgf/2020049.

Michel, S., J. Avouac, R. Jolivet, and L. Wang, 2018, Seismic and Aseismic Moment Budget and Implication for the Seismic Potential of the Parkfield Segment of the San Andreas Fault, Bull. Seismol. Soc. Am., 108, no. 1, 19–38, doi: 10.1785/0120160290.

Michel, S., R. Jolivet, C. Rollins, J. Jara, and L. Dal Zilio, 2021, Seismogenic Potential of the Main Himalayan Thrust Constrained by Coupling Segmentation and Earthquake Scaling, Geophys. Res. Lett., 48, no. 13, 1–10, doi: 10.1029/2021GL093106.

Molnar, P., 1979, Earthquake Recurrence Intervals and Plate Tectonics, 115–133.

Nivière, B., A. Bruestle, G. Bertrand, S. Carretier, J. Behrmann, and J.-C. Gourry, 2008, Active tectonics of the southeastern Upper Rhine Graben, Freiburg area (Germany), Quat. Sci. Rev., 27, nos. 5–6, 541–555, doi: 10.1016/j.quascirev.2007.11.018.

Oleskevich, D. A., R. D. Hyndman, and K. Wang, 1999, The updip and downdip limits to great subduction earthquakes: Thermal and structural models of Cascadia, south Alaska, SW Japan, and Chile, J. Geophys. Res. Solid Earth, 104, no. B7, 14965–14991, doi: 10.1029/1999JB900060.

Rollins, C., and J. Avouac, 2019, A Geodesy- and Seismicity-Based Local Earthquake Likelihood Model for Central Los Angeles, Geophys. Res. Lett., 46, no. 6, 3153–3162, doi: 10.1029/2018GL080868.

Rotstein, Y., and M. Schaming, 2011, The Upper Rhine Graben (URG) revisited: Miocene transtension and transpression account for the observed first-order structures, Tectonics, 30, no. 3, n/a-n/a, doi: 10.1029/2010TC002767.

Rouland, D., H. Haessler, K. P. Bonjer, B. Gilg, D. Mayer-Rosa, and N. Pavoni, 1983, The Sierentz Southern-Rhinegraben Earthquake of July 15, 1980. Preliminary Results, in *Developments in Solid Earth Geophysics*, 441–446.

Ruina, A., 1983, Slip instability and state variable friction laws, J. Geophys. Res. Solid Earth, 88, no. B12, 10359–10370, doi: 10.1029/JB088iB12p10359.

Steer, P., M. Simoes, R. Cattin, and J. B. H. Shyu, 2014, Erosion influences the seismicity of active thrust faults, Nat. Commun., 5, no. 1, 5564, doi: 10.1038/ncomms6564.

Stirling, M., T. Goded, K. Berryman, and N. Litchfield, 2013, Selection of Earthquake Scaling Relationships for Seismic-Hazard Analysis, Bull. Seismol. Soc. Am., 103, no. 6, 2993–3011, doi: 10.1785/0120130052.

Stucchi, M. et al., 2013, The SHARE European Earthquake Catalogue (SHEEC) 1000–1899, J. Seismol., 17, no. 2, 523–544, doi: 10.1007/s10950-012-9335-2.

Traversa, P., D. Baumont, K. Manchuel, E. Nayman, and C. Durouchoux, 2018, Exploration tree approach to estimate historical earthquakes Mw and depth, test cases from the French past seismicity, Bull. Earthq. Eng., 16, no. 6, 2169–2193, doi: 10.1007/s10518-017-0178-7.

Wells, D. L., and K. J. Coppersmith, 1994, New empirical relationships among magnitude, rupture length, rupture width, rupture area, and surface displacement, Bull. Seismol. Soc. Am., 84, no. 4, 974–1002, doi: https://doi.org/10.1785/BSSA0840040974.

Weng, H., and H. Yang, 2017, Seismogenic width controls aspect ratios of earthquake ruptures, Geophys. Res. Lett., 44, no. 6, 2725–2732, doi: 10.1002/2016GL072168.

Wesnousky, S. G., 2006, Predicting the endpoints of earthquake ruptures, Nature, 444, no. 7117, 358–360, doi: 10.1038/nature05275.

Woessner, J. et al., 2015, The 2013 European Seismic Hazard Model: key components and results, Bull. Earthq. Eng., 13, no. 12, 3553–3596, doi: 10.1007/s10518-015-9795-1.

Zaliapin, I., and Y. Ben-Zion, 2013, Earthquake clusters in southern California I: Identification and stability, J. Geophys. Res. Solid Earth, 118, no. 6, 2847–2864, doi: 10.1002/jgrb.50179.

https://doi.org/10.5194/egusphere-2023-359
Preprint. Discussion started: 13 June 2023


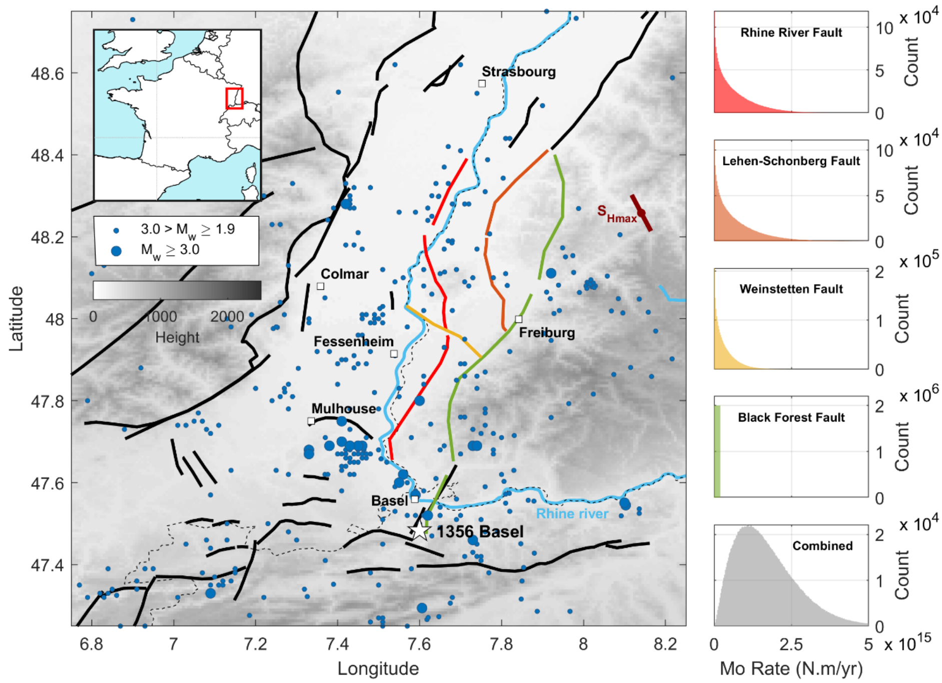


**Figure 1: (Left panel) Regional setting and seismicity of the Upper Rhine Graben (Drouet et al., 2020). Black lines are faults while colored ones are the faults taken into account in this study. The fault network geometry is based on the BDFA database (Jomard et al., 2017) and Nivière et al. (2008). Blue dots are epicenters of $M_w > 2.2$ earthquakes since 1994. The white star indicates the 1356 Basel earthquake (magnitude ranging from M6.5+/-0.5 (Manchuel et al., 2017) to M6.9+/-0.2 (Fäh et al., 2009)). The brown bar indicates the approximate orientation of the maximum horizontal compressional stress ($S_{Hmax}$) (Heidbach et al., 2016, 2018). The thin dashed black line is the border between France and Germany. The nuclear powerplant of Fessenheim and the main cities are indicated by white squares. (Right panels) Moment deficit rate PDF (expressed in counts) of each four considered fault (colors are indicative of the faults in the left panel), and of their combination (in grey).**

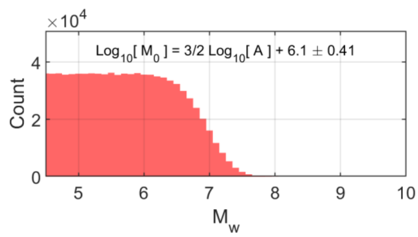


**Figure 2: PDF of $M_w$ considering the along-dip moment-area scaling law of earthquakes from Leonard (2010). Note that the area from the Black Forest Fault is not included, as its loading rate is assumed equal to 0 mm/yr.**

https://doi.org/10.5194/egusphere-2023-359
Preprint. Discussion started: 13 June 2023


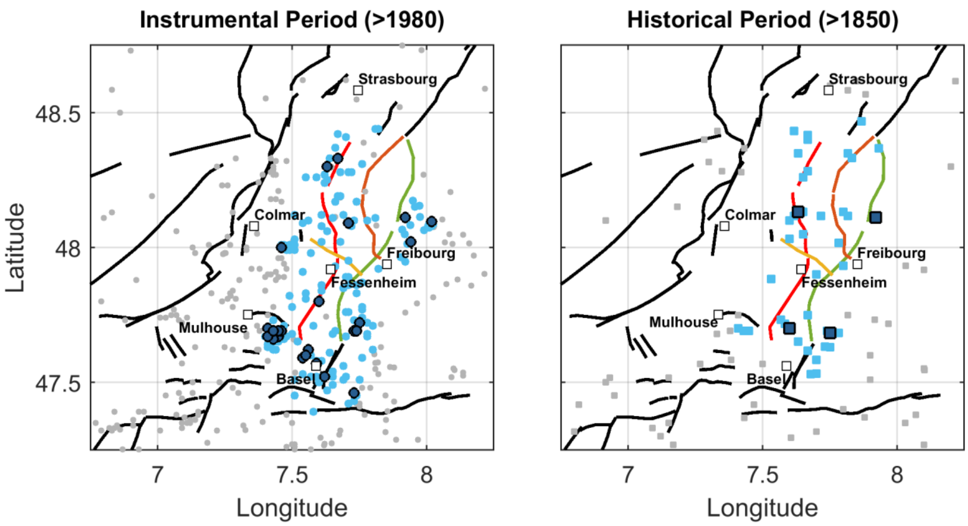


**Figure 3: Earthquake selection for the instrumental (>1994) and historical (>1850) periods. Gray dots and squares indicate all earthquakes with $M_c = 2.2$ and 3.2 for the instrumental and historical catalogs, respectively. Light blue dots and squares indicate earthquakes taken into account for the seismogenic potential analysis. Dark blue dots and squares indicate $M_w > 2.75$ and 4.25 earthquakes taken into account for the seismogenic potential analysis.**

https://doi.org/10.5194/egusphere-2023-359
Preprint. Discussion started: 13 June 2023


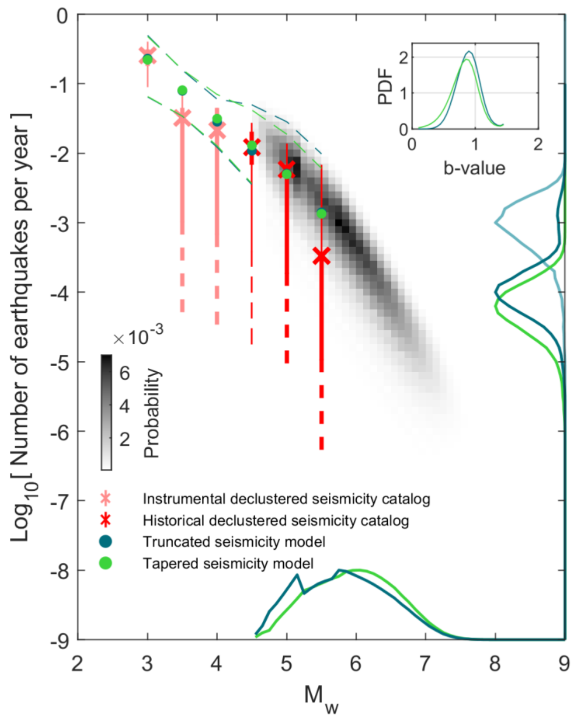


**Figure 4: Seismogenic potential of the URG using all constraints: moment budget, observed magnitude-frequency distribution, and moment area scaling law. The rate of occurrence of historical and instrumental earthquakes, within their observation period, are indicated by red and pink crosses and error bars, respectively. Thick and thin error bars indicate the 15.9-84.1% (1-sigma) and 2.3-97.7% (2-sigma) quantile of the MFDs. Dashed lines show the spread of possible MFDs for the 2500 catalogs randomly generated to explore uncertainties. The green and blue colors are associated to the tapered and truncated long-term seismicity model. Green and blue dots show the mean of the marginal PDF of the long-term seismicity. Green and blue dashed lines indicate the spread of the 1% best seismicity models. The marginal probabilities of $M_{max}$, $P_{M_{max}}$, are indicated by the solid lines on the $M_w$ axis . Green and dark blue lines on the earthquake frequency axis indicate the probability of the rate of events, $\tau$, with magnitude $M_w = M_{Mode}$, thus $P(\tau \mid M_w = M_{Mode})$, with $M_{Mode}$=6.05 and 5.75 for the tapered and truncated models, respectively, considering all magnitudes in the seismicity models and not only the recurrence rate of $M_{max}$. Light blue line on the earthquake frequency axis indicates $P(\tau_{max} \mid M_{max} = 5.75)$ (only for the truncated seismicity model). The top-right inset shows the marginal probability of the b-value. Note that the seismicity MFDs in the figure are not in the cumulative form.**

https://doi.org/10.5194/egusphere-2023-359
Preprint. Discussion started: 13 June 2023


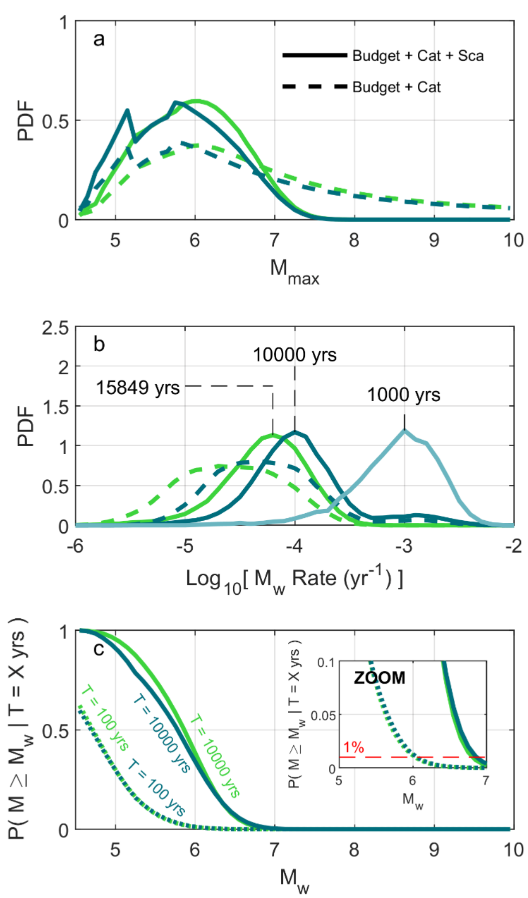


**Figure 5: (a) Evolution of the marginal PDF of $M_{\max}$ when adding the moment-area scaling law constraint. The green and blue colors in the figure are associated to the tapered and truncated long-term seismicity model. (b) Same as (a) but for the marginal PDF of the recurrence time of events: $P(\tau \mid M_w = 6.05)$ and $P(\tau \mid M_w = 5.75)$ for the tapered and truncated models (dark blue and green lines), respectively, and $P(\tau_{max} \mid M_{max} = 5.75)$ shown only for the truncated model (light blue solid line). (c) Probability of occurrence of earthquakes of magnitude larger than $M_w$ over a period of X yrs. We show the probability of occurrence of such events for the 100 yrs and 10,000 yrs time periods. In (a), (b) and (c), dotted lines represent the marginal PDFs considering both the moment budget and seismicity catalog constraint, the dashed lines indicate the PDFs when adding the earthquake scaling constraint. The inset in (c) is a zoom of the panel. The 1% probability of exceedance over a time period of 100 yrs is a typical order of magnitude for nuclear application in France.**

https://doi.org/10.5194/egusphere-2023-359
Preprint. Discussion started: 13 June 2023


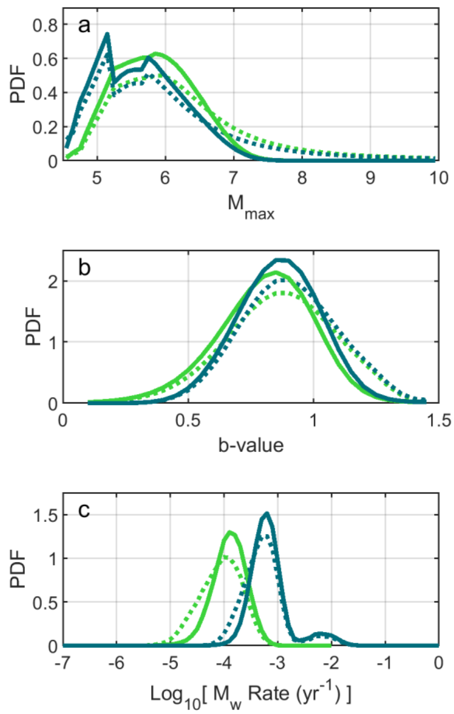


**Figure 6: Results using the declustering method from Zaliapin and Ben-Zion (2013) instead of Marsan et al. (2017) (Text S2). In this scenario, no probabilities of events to be mainshocks are defined. (a) $M_{max}$ PDF. (b) b-value PDF. (c) $P(\tau \mid M_w = M_{Mode})$ PDF. Solid lines correspond to the results using all constraints while the dotted lines use only the moment budget and earthquake catalogs constraints. Green and blue lines correspond to the tapered and truncated models, respectively. The results shown here are the ones taking a b-value equal to 1 for Zaliapin and Ben-Zion (2013) declustering method. The results for b-values of 0.5 and 1.5 are also shown in Figure S11 and are relatively similar to the ones using a b-values of 1.0.**

https://doi.org/10.5194/egusphere-2023-359
Preprint. Discussion started: 13 June 2023


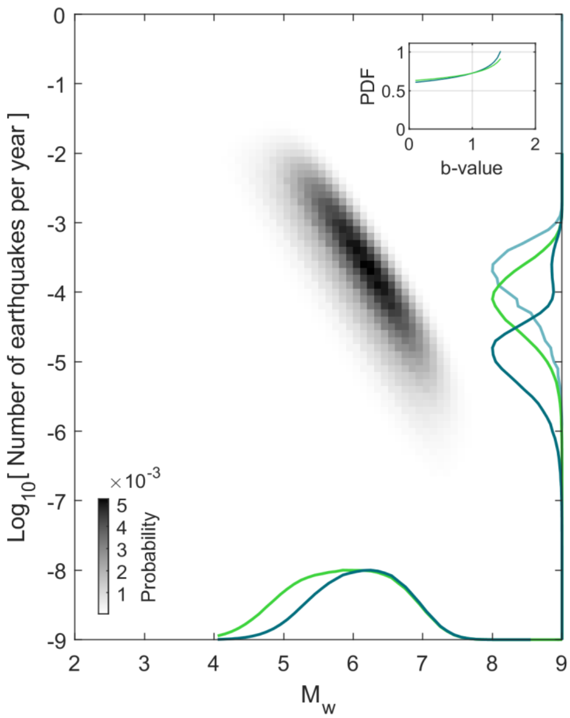


**Figure 7: Same as Figure 4 but considering only the constraints on the moment budget, the moment-area scaling law, and the one on $M_{max}$ frequency considering the time period of the catalog (which serves as a lower bound constraint to $M_{max}$; Section 5.2; Approach 2 from Michel et al., 2018).**

https://doi.org/10.5194/egusphere-2023-359
Preprint. Discussion started: 13 June 2023


589 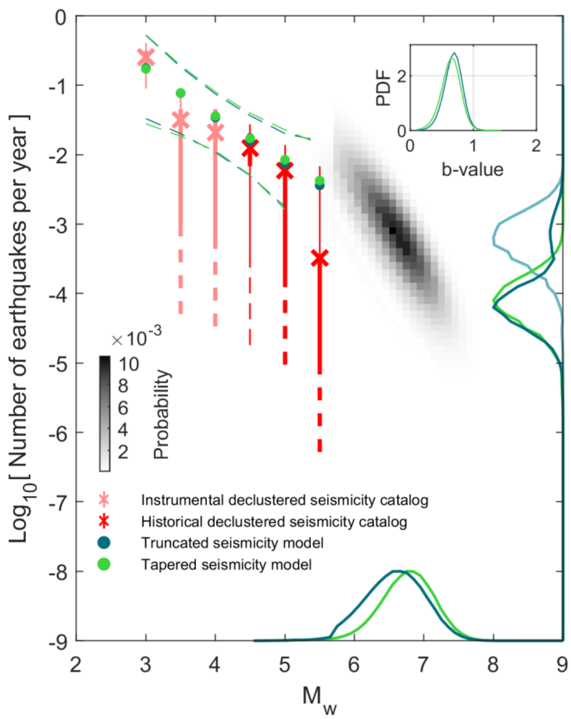


590 **Figure 8: Same as Figure 2 but considering a strike-slip slip rate component equivalent to 6.6 times the dip-slip estimate,**
591 **and assuming the Black Forest Fault maximum long-term vertical slip rate is 0.18 mm/yr (as proposed by Jomard et**
592 **al., 2017). Leonard et al. (2010) strike-slip moment-area scaling law is used here for the scaling law constraint, even**
593 **though it is very similar to the dip-slip version.**

594

https://doi.org/10.5194/egusphere-2023-359
Preprint. Discussion started: 13 June 2023


**Table 1: Fault parameters. $\mathcal{U}$ and $\mathcal{N}$ stands for uniform and normal distribution. The PDFs of each of those parameters and the resulting moment deficit rate of each fault are shown in Figure S2 to S5.**

| **Fault Name** | **Segment Name (from BDFA)** | **Dip (°)** | **Length (km)** | **Slip-Rate (mm/yr)** | **Seismogenic zone down-dip extent (km)** | **Evaporite layer thickness (km)** |
|---|---|---|---|---|---|---|
| Rhine River Fault | FRR-1 | $\mathcal{U}(50,80)$ | $\mathcal{N}(35,2)$ | $\mathcal{U}(0,0.07)$ | (1) Uniform from 0 to 6 km depth. (2) Linearly decreasing from 6 to 18 km depth. | $\mathcal{U}(0,2)$ |
| | FRR-2 | $\mathcal{U}(50,80)$ | $\mathcal{N}(25,2)$ | | | |
| | FRR-3 | $\mathcal{U}(55,85)$ | $\mathcal{N}(20,2)$ | | | |
| Black Forest Fault | FFN-1 | $\mathcal{U}(35,75)$ | $\mathcal{N}(20,5)$ | 0 | | |
| | FFN-2 | $\mathcal{U}(40,80)$ | $\mathcal{N}(50,2)$ | | | |
| | FFN-3 | $\mathcal{U}(35,75)$ | $\mathcal{N}(35,2)$ | | | |
| Lehen-Schonberg | | $\mathcal{U}(40,80)$ | $\mathcal{N}(54,2)$ | $\mathcal{U}(0,0.1)$ | Does not apply to the Black Forest Fault as its loading rate is assumed equal to 0 mm/yr | |
| Weinstetten | | $\mathcal{U}(40,80)$ | $\mathcal{N}(15,2)$ | $\mathcal{U}(0,0.17)$ | | |